Electronic Supplementary Information

Quantitative Analyses of Enhanced Thermoelectric Properties of Modulation-Doped PEDOT:PSS / Undoped Si (001) Nanoscale Heterostructures

Dongwook Lee[a], Sayed Youssef Sayed[b, c, ‡], Sangyeop Lee[b, ‡], Chris Adam Kuryak[b], Jiawei Zhou[b], Gang Chen[b, *], and Yang Shao-Horn[a, b, c, *]

a. Department of Materials Science and Engineering, Massachusetts Institute of Technology, Cambridge, Massachusetts, United States, 02139

b. Department of Mechanical Engineering, Massachusetts Institute of Technology, Cambridge, Massachusetts, United States, 02139

c. The Research Laboratory of Electronics, Massachusetts Institute of Technology, Cambridge, Massachusetts, United States, 02139

‡These authors contributed equally.

Sequence of Thermoelectric Performance Measurements

As PEDOT:PSS is easily damaged upon mechanical contacts, measurements with less contact with samples were conducted earlier. Hence, AFM measurement was conducted first, followed by Seebeck coefficient measurements, 4-point probe electrical conductivity measurements, and PEDOT:PSS thickness measurements.

Seebeck Coefficient Measurements[1]

The Seebeck coefficient (S) of all samples was measured with a lab-made setup. In order to determine the Seebeck coefficient, it was necessary to induce a temperature gradient across the sample and measure the voltage change (ΔV) and temperature difference (ΔT). To accomplish this, a Seebeck measurement device was built (Figure S1). The device used two commercially available Peltier modules (TE Technology, Inc.) to heat up one side of the sample and cool down the opposite side. Current was applied through the Peltier heaters in opposite directions using a current source (Keithley 2400), which made one device a heater and the other a cooler. Under each Peltier heater/cooler was a small heat sink to help conduct heat and create the largest possible temperature difference across the heater or cooler. The sample and alumina support bridged the gap between the heater and cooler.

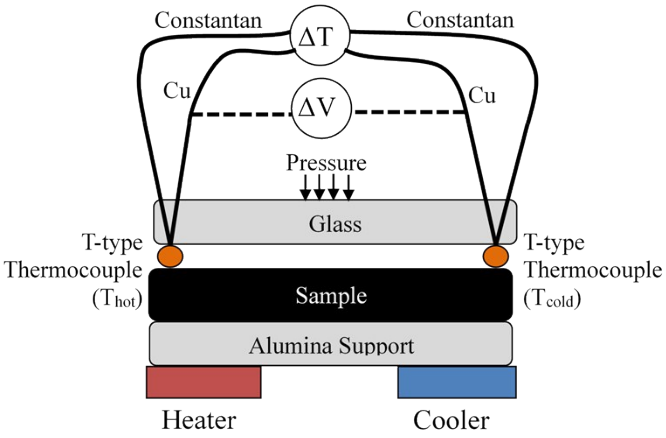

Figure S1. Schematic diagram of Seebeck coefficient measurement setup. The Peltier plates provide a temperature gradient across the sample. The temperature and voltage are measured at the same position, by two T-type thermocouples. Pressure is provided on the thermocouples to maintain firm electrical and thermal contacts with the sample.

Electrical Conductivity Measurements by 4-point Probe and Hall Techniques

Electrical conductivity was measured by 4-point probe method (LucasLabs Pro4). To obtain a more accurate electrical conductivity measurement, 9 individual measurements were taken on each sample. These 9 measurements were averaged together to develop the reported electrical conductivity of the samples.

Hall measurements (LakeShore 7500 Series Hall System) were also adopted limitedly only to assess mobility of PEDOT:PSS film on SiO_2, as displayed at Figure S9. Those measurements yielded similar results to each other: for instance, electrical conductivity of 2.0 μm thick PEDOT:PSS on SiO_2 was 537.12 S/cm by 4-point probe measurement, and 501.88 S/cm by Hall measurement. The difference between the two measurements is less than 7 %.

PEDOT:PSS Thickness Measurements with AFM

The thickness of each sample was measured with AFM using a Veeco NanoScope IV. To obtain an estimate of the thickness, 2 lines were scratched onto the sample using a razor blade thereby exposing the substrate underneath. The step heights were measured at each of these scratches (Figure S2), and averaged values were employed as PEDOT:PSS thickness of each sample.

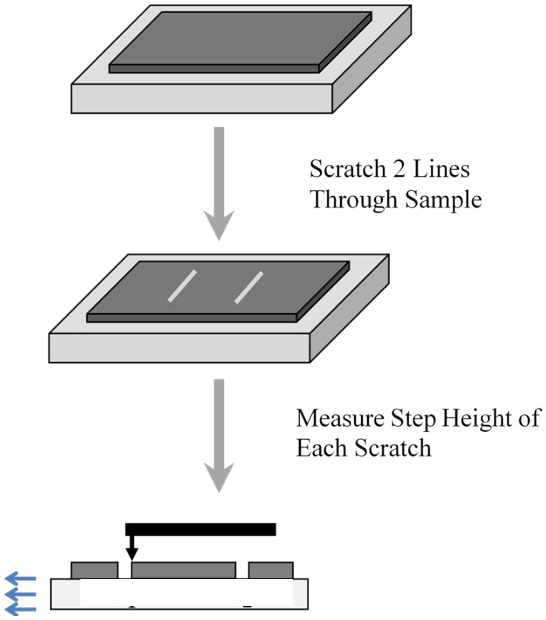

Figure S2. The procedure for thickness measurements using the AFM.

Si and SiO_x Thickness Measurements by X-ray Reflectivity (XRR)

Thickness of SiO_x layer on Si after oxide strip or generation chemical process, was examined by XRR measurements. Thickness of Si layer on sapphire after thermal oxidation and following HF etching was also determined by XRR measurements. This technique utilizes that the length of interference path depends on incident angle of the electromagnetic wave (X-ray). Therefore, the intensity of the reflected beam will have periodic rise and fall, imposed by boundary conditions, such as wavelength of the incident beam, densities and thicknesses of the films. Since the wavelength of the beam is fixed at that of Cu K α (0.15418 nm), analysis of the periodic interference pattern measured by XRR informs thickness of the thin film. Beam size was consistently 5×5 mm^2 for all XRR measurements. Figure S3 represents an exemplar XRR pattern of thermally oxidized and then HF etched SOS.

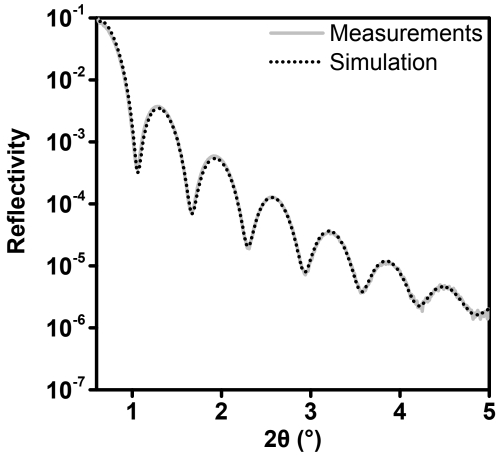

Figure S3. An exemplar interference pattern of 14 nm thick Si on sapphire measured by XRR.

Effect of Chemical Treatments on Thickness of SiO_x on SOS

SiO_x on Si is inevitable in order to accommodate PEDOT:PSS on Si surface. On the other hand, SiO_x thickness should be minimized since SiO_x can complicate analysis and modelling for numerical simulation. Exposing the etched surface to 10 vol% piranha satisfies those two conflicting requirements by creating a hydrophilic surface to deposit PEDOT:PSS (Figure 1c), as well as generating sub-nanometer thick SiO_x layer (Figure S4).

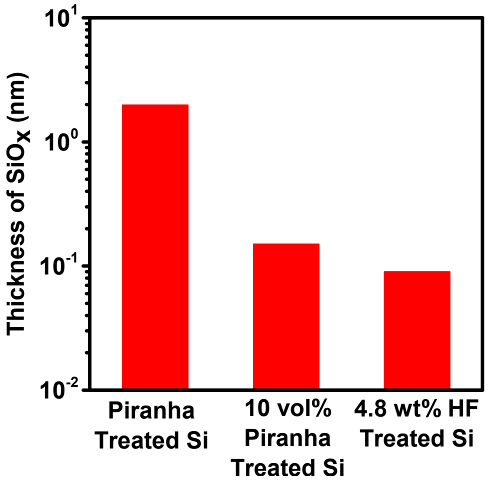

Figure S4. Thicknesses of SiO_x on Si by varying chemical treatments on SOS wafers, measured with XRR.

Thermal Oxidation of SOS for Silicon Thickness Control

Thermal oxidation of SOS was introduced in order to decrease the thickness of the Si layer. It converts Si into SiO_2 from the interface with air at certain rate under specific temperature, humidity, and crystalline orientation[2]. SiO_x was removed after thermal oxidation with HF etching.

Before thermal oxidation RCA 1 and RCA 2 cleaning procedures were conducted in order to minimize the introduction of metallic elements to Si[2], which could turn into dopants after thermal oxidation. For this study, we used dry oxidation at 1100 ^{o}C for varying time duration for (001) SOS under 40 mL/s of dry oxygen flow, as high temperature at 1100 ^{o}C ensures quick oxidation, and dry condition tend to produce atomically flat surface[2]. Figure S5 shows morphology of the resultant SOS after thermal oxidation, and resultant resistivity of thinned down SOS. The thermal growth of SiO_2 layer followed established empirical trend[2], which is summarized at Figure S6.

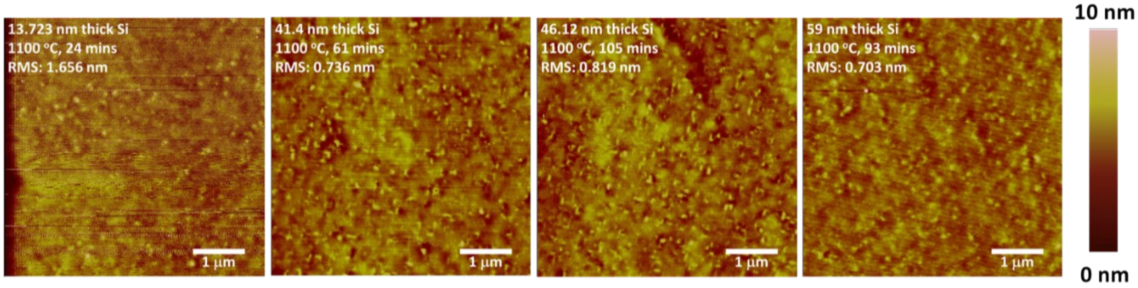

Figure S5. Surface roughnesses of Si were kept flat even after thermal oxidation at 1100 ^{o}C for varying durations, and following HF removal of thermally grown SiO_x.

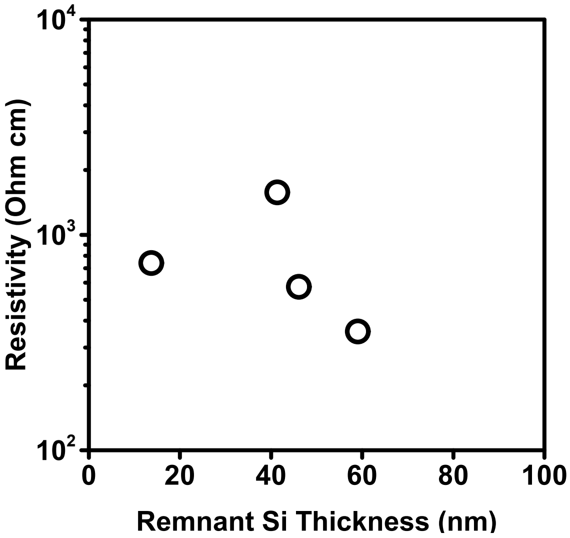

Figure S6. Resultant resistivity of SOS after thermal oxidation and subsequent HF etching. Resistivity remained highly intrinsic even after the thermal oxidation.

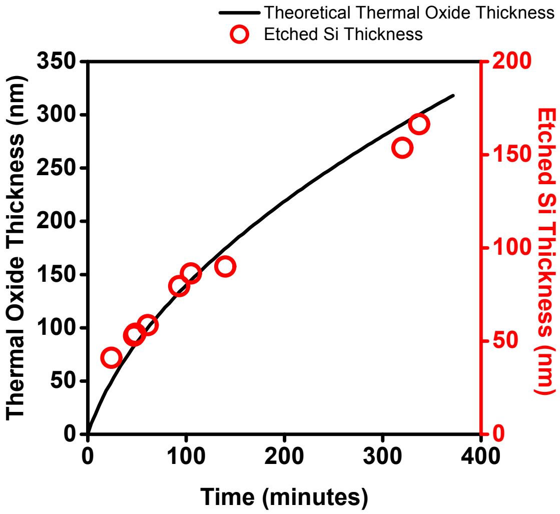

Figure S7. Thermal growth of SiO_2 on (001) Si shows agreement with theoretical Deal-Grove model, where oxygen gas diffuses from the outside to the surface, then through the existing oxide layer to the oxide-substrate interface, and then lastly reacts with buried Si atoms[2].

Dependence of Sheet Resistance on Combined Thickness of PEDOT:PSS and Si

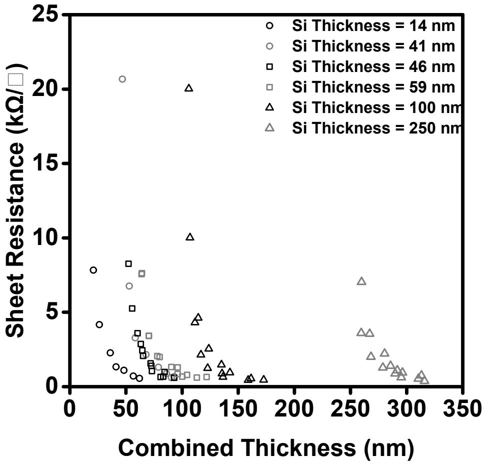

Figure S8. Sheet resistances of PEDOT:PSS / Si heterostructure. The sheet resistance mainly depends on PEDOT:PSS thickness, not Si thickness. Almost identical trends are shifted horizontally due to different Si thicknesses. Black circles, grey circles, black squares, grey squares, black triangles, and grey triangles correspond to 14 nm, 41 nm, 46 nm, 59 nm, 100 nm, and 250 nm of Si thicknesses, respectively.

Evolution of Electrical Conductivity and Mobility of PEDOT:PSS on SiO_2 Quartz by Variation of Thickness

Thickness dependence of electrical conductivity of thin films on insulating substrate is a general phenomenon for various materials[3-5]. Especially for PEDOT:PSS thin films on various insulating substrates, increase in film thickness accompanies increase in film thickness[6, 7]. Measured electrical conductivity of PEDOT:PSS on SiO_2 quartz substrate shares the similar trends for investigated range of thickness (5 – 60 nm), as shown in Figure S9. It should be noted that linear fitting of PEDOT:PSS electrical conductivity evolution does not have theoretical basis so far. This linear fitting was adopted only to provide an estimation of PEDOT:PSS electrical conductivity trend within the researched thickness region in this study.

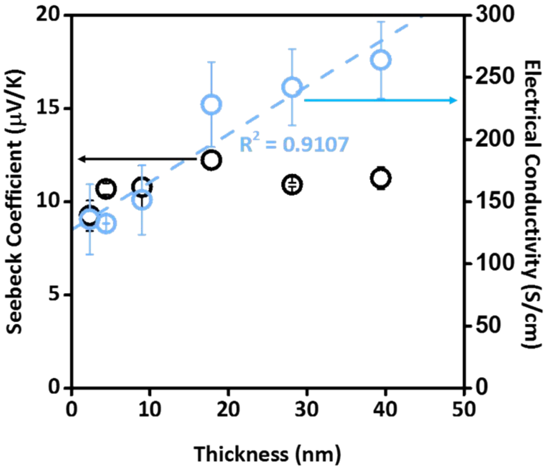

Figure S9. Electrical conductivity of PEDOT:PSS on SiO_2 quartz with linear fitting. Note that linear trend does not have theoretical justification. Seebeck coefficient of PEDOT:PSS on SiO_2 quartz is constant, which evidences hole density of PEDOT:PSS is invariant.

Distinguishing mobility and hole density from electrical conductivity is necessary to solve Poisson's equation. However, it has been widely reported that low mobility of PEDOT:PSS[8, 9] renders Hall measurement technically difficult[10]. Only for PEDOT:PSS on SiO_2 with micron-scale thickness (6.78 μm), linear relation between Hall voltage and applied external magnetic field could be found, as shown in Figure S10. PEDOT:PSS with less thickness failed to produce clear linear relation, therefore mobility and hole density could not be measured for that range of thickness. Mobility and hole density could be obtained by following formulas, as indicated below, where n, μ, σ, e, d, and a represent hole density, mobility, electrical conductivity, elementary charge, thickness of PEDOT:PSS, and slope of Figure S10.

$$n = \frac{1}{aed} \tag{S1}$$

$$\mu = \frac{\sigma}{ne} \tag{S2}$$

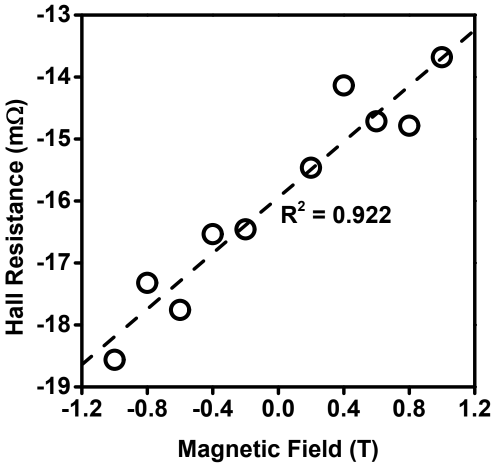

Figure S10. Hall resistance showed a linear relationship with applied external magnetic field, only when thickness of PEDOT:PSS on SiO_2 was in micrometer range. For PEDOT:PSS with nanometer scale thickness, trends were completely noisy.

Therefore, it could be concluded that mobility and hole density of 6.78 μm thick PEDOT:PSS are 7.90 $cm^2/V{\cdot}s$ and 4.16×10^{20} cm^{-3}, respectively. The measured hole density of PEDOT:PSS is at similar range with previously reported values[11].

Even though direct measurement of hole density was not possible for PEDOT:PSS with less than μm scale, it was still possible to draw hole density from Seebeck coefficient measurement. Seebeck coefficient of PEDOT:PSS strictly is only affected by hole density, as reported in a previous research[7, 12].

Combined with constant Seebeck coefficient trend of PEDOT:PSS at Figure S9, it can be concluded that hole density of PEDOT:PSS stays the same as well. Given that electrical conductivity of PEDOT:PSS depends on thickness, then it is mobility that varies with thickness. This result was employed as input parameters for Poisson's equation.

Band Alignment of PEDOT:PSS Thin Film on Si with Varying Thicknesses

The numerical simulation of Poisson's equation by COMSOL Multiphysics® Modeling Software analyzed band bending at equilibrium after the heterojunction formation, for various thicknesses of (001) Si (Figure S11). Band bending does not happen at PEDOT:PSS layer, as PEDOT:PSS has nearly metallic hole density. At the Si side close to the interface, the band offset and band bending is preserved regardless of Si thicknesses. This implies no significant change in Seebeck coefficient trend, since the contribution to Seebeck coefficient from the region far from the interface is negligible, as explained in the main text.

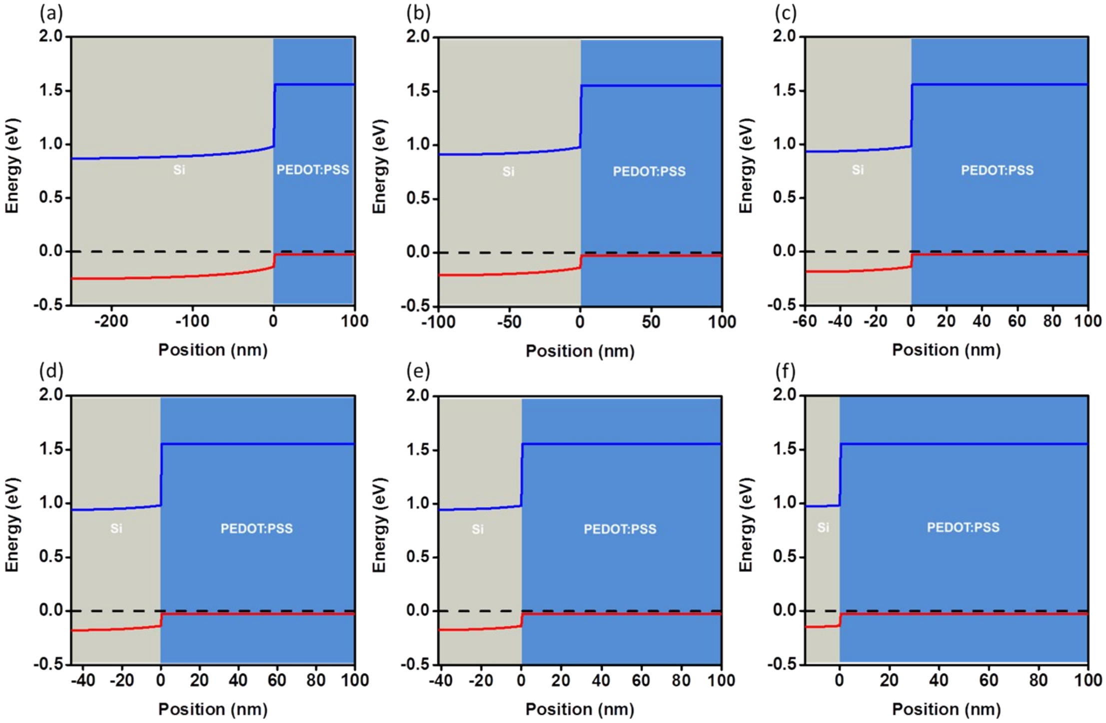

Figure S11. (a) – (f) Band diagrams of PEDOT:PSS / Si heterojunction at 250 nm, 100 nm, 59 nm, 46 nm, 41 nm, and 14 nm thick Si.

Modeling of the Seebeck Coefficient and Electrical Conductivity: without Band Bending

As explained in the main text, parallel resistor model was assumed to estimate theoretical Seebeck coefficient and electrical conductivity. When no band bending upon contact between PEDOT:PSS and Si is assumed, charge distribution within PEDOT:PSS and Si will be unchanged. This means Seebeck coefficient and electrical conductivity of PEDOT:PSS and Si will stay the same. Therefore, theoretical Seebeck coefficient and electrical conductivity of PEDOT:PSS / Si heterostructure can be expressed by following formalism:

$$\frac{1}{\bar{R}} = \frac{1}{R_1} + \frac{1}{R_2} \qquad \text{(S3)}$$

$$\bar{\sigma}(d_1 + d_2)\frac{w}{l} = \sigma_1 d_1 \frac{w}{l} + \sigma_2 d_2 \frac{w}{l} \qquad \text{(S4)}$$

$$\bar{\sigma} = \frac{\sigma_1 d_1 + \sigma_2 d_2}{d_1 + d_2}$$

(S5)

$$\frac{\bar{S}}{\bar{R}} = \frac{S_1}{R_1} + \frac{S_2}{R_2} \qquad \text{(S6)}$$

$$\bar{\sigma}\bar{S}(d_1 + d_2)\frac{w}{l} = \sigma_1 S_1 d_1 \frac{w}{l} + \sigma_2 S_2 d_2 \frac{w}{l} \qquad \text{(S7)}$$

$$\bar{S} = \frac{S_1 \sigma_1 d_1 + S_2 \sigma_2 d_2}{\sigma_1 d_1 + \sigma_2 d_2} \qquad \textbf{(S8)}$$

where R_1, R_2, d_1, d_2, σ_1, σ_2, S_1, and S_2 represent resistance, thickness, electrical conductivity, and Seebeck coefficient of Si and PEDOT:PSS respectively. w and l mean width and length of the sample, which always were 1.0 cm. $\bar{\sigma}$ and $\bar{S}$ are electrical conductivity and Seebeck coefficient of PEDOT:PSS / Si heterostructure.

Modeling of the Seebeck Coefficient and Electrical Conductivity with Band Bending

When band bending is assumed, valence band edge at each position changes, as shown in Figure S11. The band bending causes different hole density at each position. Therefore hole density at certain position can be converted to electrical conductivity and Seebeck coefficient at corresponding position. Charge scattering mechanism in PEDOT:PSS and Si were regarded the same even after modulation doping, leading to preserved mobility of holes in Si and PEDOT:PSS. Pisarenko relation of PEDOT:PSS[12] and (001) Si[13-16] at room temperature were adopted to evaluate Seebeck coefficient at specific hole density. Detailed mathematical expressions are shown below:

$$\sigma_1(n_1(x)) = n_1(x)e\mu_1 \tag{S9}$$

$$\sigma_2(n_2(x)) = n_2(x)e\mu_2 \tag{S10}$$

$$S_1(n_1(x)) = \frac{k_B}{e}(\ln\left(\frac{N_{V1}}{n_1(x)}\right) + 3) \quad \text{at room temperature} \tag{S11}$$

where μ_1 and μ_2 are the mobility of holes in Si and PEDOT:PSS layer, N_{V1} the valence band density of states of Si, k_B the Boltzmann constant, e the elementary charge, respectively. Hole density dependent Seebeck coefficient of PEDOT:PSS, $S_2(n_2(x))$, was taken from Pisarenko plot in the previous research[12].

In order to evaluate the overall sample thermoelectric properties, averaging the Seebeck coefficient and electrical conductivity over the entire thickness of PEDOT:PSS and Si were needed. Parallel resistor model was applied and each position was regarded as a resistor. Detailed mathematical expressions are shown below.

$$\frac{1}{R} = \sum_i \frac{1}{R_i} \tag{S12}$$

$$\bar{\sigma} = \frac{\int_{-d_1}^{0} n_1(x) e\mu_1 dx + \int_{0}^{d_2} n_2(x) e\mu_2 dx}{d_1 + d_2} \tag{S13}$$

$$\bar{S} = \frac{\int_{-d_1}^{0} S_1(x) n_1(x) e\mu_1 dx + \int_{0}^{d_2} S_2(x) n_2(x) e\mu_2 dx}{\bar{\sigma}(d_1 + d_2)} \tag{S14}$$

where $R_i$is resistance of individual infinitesimal resistors, $\bar{R}$, $\bar{\sigma}$, and $\bar{S}$ represent resistance, thickness, electrical conductivity, and Seebeck coefficient of overall samples, respectively.

Power Factors at Various Si Thicknesses

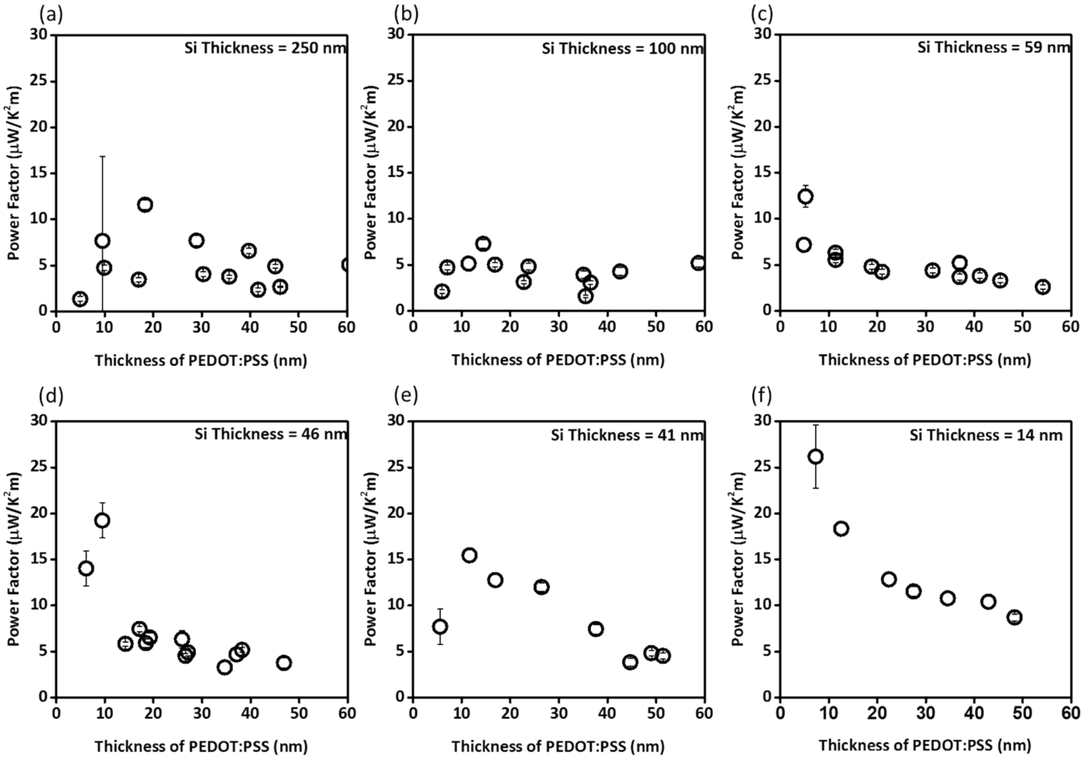

Figure S12. (a) – (f) Power factors of PEDOT:PSS films of different thicknesses on 250 nm, 100 nm, 59 nm, 46 nm, 41 nm, and 14 nm thick Si, respectively. These are estimated from multiplying individually measured Seebeck coefficients and electrical conductivities.

Power Factors at Various Combined Si and PEDOT:PSS Thicknesses

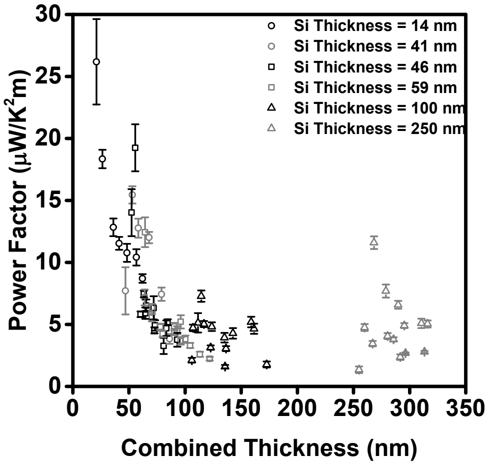

Figure S13. Power factors of PEDOT:PSS / Si heterostructure consistently increases as combined thickness of the heterostructure decreases. Decreasing Si thickness improves electrical conductivity by reducing portion of undoped Si far from the interface for electrical conductivity normalization. Reducing PEDOT:PSS thickness sacrifices electrical conductivity, while Seebeck coefficient increases. Those trends are reflected in this plot. Black circles, grey circles, black squares, grey squares, black triangles, and grey triangles correspond to 14 nm, 41 nm, 46 nm, 59 nm, 100 nm, and 250 nm of Si thicknesses, respectively.

UV – Vis - NIR Spectra of 6.5 nm PEDOT:PSS, 14 nm SOS, and 6.5 nm PEDOT:PSS on 14 nm SOS

It has been known that when PEDOT:PSS undergoes doping / dedoping by chemical treatments, such as application of solvents, its transmission pattern changes, as dominant transitions between its subbands alters their probabilities[12]. UV – Vis – NIR was employed to determine if 6.5 nm thick PEDOT:PSS on 14 nm thick SOS and bulk SiO_2 exhibits different doping state (Figure S14). Because the absorption is mostly governed by SOS, it is not possible to clarify PEDOT:PSS doping state dependence on substrates.

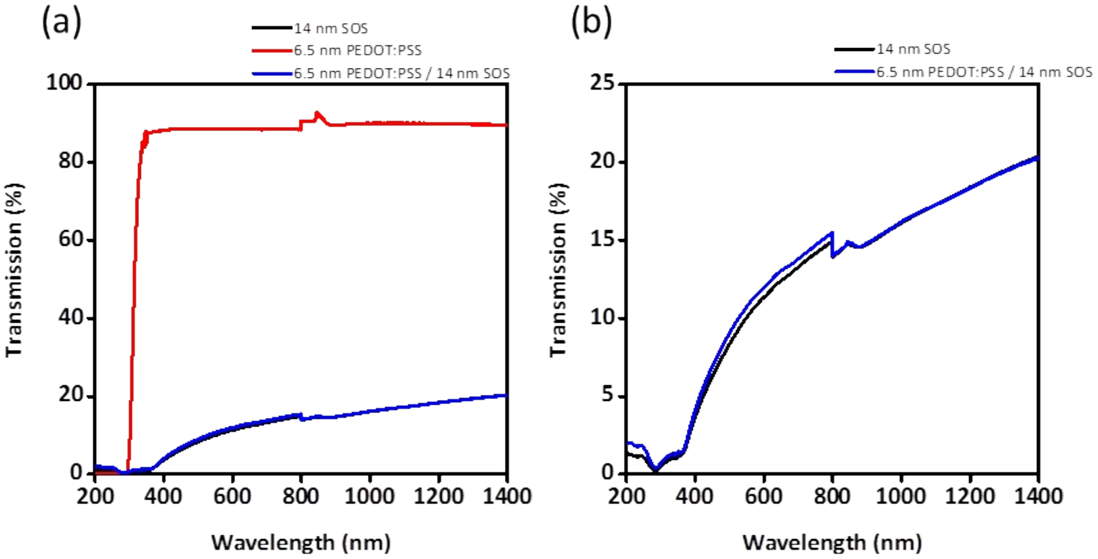

Figure S14. Transmission spectra at UV-Vis-NIR wavelength region of 14 nm thick SOS, 6.5 nm thick PEDOT:PSS on bulk SiO_2, and 6.5 nm thick PEDOT:PSS on 14 nm thick SOS.

Preferred Orientation of PEDOT:PSS

It is very plausible for PEDOT:PSS thin film on Si and SiO_2 to have preferred orientations. Adoption of co-solvents, such as ethanol and DMSO so far proved effective to align nanoscale grains of PEDOT favorable for hole conduction[17-19], as it realigns to enhance hole hopping rate from PEDOT nanograin to another[17], thereby improving mobility of holes in PEDOT:PSS. This is another reason why we also adopted mixture of PEDOT:PSS with co-solvents of ethanol and DMSO, in addition to wettability issue on Si surface.

References

1. C. A. Kuryak, *Nanostructured thin film thermoelectric composite materials using conductive polymer PEDOT:PSS*, c2013., 2013.
2. G. E. McGuire, *Semiconductor materials and process technology handbook : for very large scale integration (VLSI) and ultra large scale integration (ULSI)*, Park Ridge, N.J., U.S.A. : Noyes Publications, c1988., 1988.
3. N. Yoshikatsu, *Japanese Journal of Applied Physics*, 1970, **9**, 1326.
4. A. F. Mayadas and M. Shatzkes, *Physical Review B*, 1970, **1**, 1382-1389.
5. K. Fuchs, *Mathematical Proceedings of the Cambridge Philosophical Society*, 1938, **34**, 100-108.
6. W. Seifert, H. Albrecht, S. Mietke, T. Kohler and M. Werner, Place of Publication: San Diego, CA, USA. Country of Publication: USA.
7. D. Yoo, W. Son, S. Kim, J. J. Lee, S. H. Lee, H. H. Choi and J. H. Kim, *RSC Advances*, 2014, **4**, 58924-58929.
8. S. A. Rutledge and A. S. Helmy, *Journal of Applied Physics*, 2013, **114**, 133708.
9. R. Coehoorn, W. F. Pasveer, P. A. Bobbert and M. A. J. Michels, *Physical Review B*, 2005, **72**.
10. L. A. Eldada, J. Lindemuth and S.-I. Mizuta, 2011, **8110**, 81100I.
11. C. Liu, B. Lu, J. Yan, J. Xu, R. Yue, Z. Zhu, S. Zhou, X. Hu, Z. Zhang and P. Chen, *Synthetic Metals*, 2010, **160**, 2481-2485.
12. O. Bubnova, M. Berggren and X. Crispin, *Journal of the American Chemical Society*, 2012, **134**, 16456-16459.
13. Z. Bian, A. Shakouri, L. Shi, H.-K. Lyeo and C. K. Shih, *Applied Physics Letters*, 2005, **87**, 053115.
14. H.-K. Lyeo, A. A. Khajetoorians, L. Shi, K. P. Pipe, R. J. Ram, A. Shakouri and C. K. Shih, *Science*, 2004, **303**, 816-818.
15. K. P. Pipe, R. J. Ram and A. Shakouri, *Physical Review B*, 2002, **66**, 125316.
16. B. Lee, K. Kim, S. Lee, J. H. Kim, D. S. Lim, O. Kwon and J. S. Lee, *Nano Lett*, 2012, **12**, 4472-4476.
17. Y. Xia and J. Ouyang, *Journal of Materials Chemistry*, 2011, **21**, 4927-4936.
18. J. P. Thomas and K. T. Leung, *Journal of Materials Chemistry A*, 2016, DOI: 10.1039/c6ta07410c.
19. E. Jin Bae, Y. Hun Kang, K.-S. Jang and S. Yun Cho, *Scientific reports*, 2016, **6**, 18805.